Raman Spectroscopy of Optical Transitions and Vibrational Energies of ~1 nm HgTe Extreme Nanowires within Single Walled Carbon Nanotubes

Joseph H. Spencer,[†] John M. Nesbitt,[†] Harrison Trewhitt,[‡] Reza J. Kashtiban,[‡] Gavin Bell,[‡] Victor G. Ivanov,[§,⊥] Eric Faulques,[⊥] Jeremy Sloan,[‡,*] and David C. Smith[†,*]

[†]School of Physics and Astronomy, University of Southampton, Southampton SO17 1BJ, United Kingdom, [‡]Department of Physics, University of Warwick, Coventry CV4 7AL, United Kingdom, [§]Faculty of Physics, Sofia University, 5 J. Bouchier Blvd., BG 1164 Sofia, Bulgaria, and [⊥]Institut des Matériaux Jean Rouxel, University of Nantes CNRS, UMR6502, F-44322 Nantes, France. The Raman spectroscopy was undertaken at the University of Southampton under the leadership of D.C.S. The samples were prepared and TEM characterized at the University of Warwick under the leadership of J.S. The DFT calculations were performed at the University of Nantes. The manuscript was written through contributions of all authors. All authors have given approval to the final version of the manuscript.

ABSTRACT This paper presents a resonance Raman spectroscopy study of ~1 nm diameter HgTe nanowires formed inside single walled carbon nanotubes by melt infiltration. Raman spectra have been measured for ensembles of bundled filled tubes, produced using tubes from two separate sources, for excitation photon energies in the ranges 3.39–2.61 and 1.82–1.26 eV for Raman shifts down to ~25 cm^{-1}. We also present HRTEM characterization of the tubes and the results of DFT calculations of the phonon and electronic dispersion relations, and the optical absorption spectrum based upon the observed structure of the HgTe nanowires. All of the evidence supports the hypothesis that the observed Raman features are not attributable to single walled carbon nanotubes, *i.e.*, peaks due to radial breathing mode phonons, but are due to the HgTe nanowires. The observed additional features are due to four distinct phonons, with energies 47, 51, 94, and 115 cm^{-1}, respectively, plus their overtones and combinations. All of these modes have strong photon energy resonances that maximize at around 1.76 eV energy with respect to incident laser.

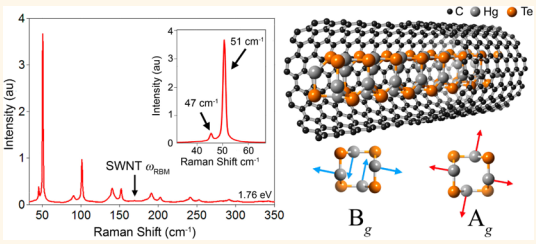

KEYWORDS: resonant Raman spectroscopy · HgTe@SWCNT · nanowires · carbon nanotubes · DFT · HRTEM

Infiltration of inorganic materials into the central pores of single walled carbon nanotubes (SWCNTs) allows the encapsulation of extreme nanowires with diameters comparable to a single unit cell of the parent material.[1,2] For SWCNTs with diameters in the range 0.8–1.6 nm, embedded nanocrystals with sterically and systematically reduced coordination are observed resulting, in some instances, in metastable crystalline forms not encountered in the bulk forms of the same material.[3,4] While comparable diameter nanowires can be produced using a range of templates including zeolites,[5] mesoporous phases,[6,7] and metal organic framework (MOF)-type materials,[8] SWCNTs have a number of advantages as templates; they are atomically smooth, electron transparent, are readily available, and can be filled easily using melt infiltration in order to create milligram quantities of encapsulated nanowires on at least a laboratory scale. Thus, encapsulated SWCNT nanowires are scientifically interesting not only in their own right but also as a pathfinder for a wide range of other extreme nanowire materials.

So far much of the work on filled carbon nanotubes has focused on establishing the range of materials that can be infiltrated and then observing the effect of confinement on the crystallography of the encapsulated materials. Less attention has been given over to their fundamental physical and functional properties. For example, while there have been a number of theoretical

* Address correspondence to dcsmith@soton.ac.uk, j.sloan@warwick.ac.uk.

Received for review April 30, 2014 and accepted August 27, 2014.

Published online August 27, 2014
10.1021/nn5023632

predictions[4] that the electronic energies of the encapsulated nanowires will be very significantly modified with respect to the bulk phases, there are few experimental studies demonstrating this to date. Another interesting area of study are phase transitions of fillings, including pressure driven phase transitions in polyiodide filled tubes[9] and bending driven transitions in AgI,[2] and recently it was observed that GeTe inside a nanotube exhibits solid-amorphous phase change behavior.[10]

The interactions between host tube and filling are also interesting. In this respect, the majority of recent studies have focused on charge transfer with both hole doping, from fillings such as iodine[11,12] and more recently graphene nanoribbons,[13] and electron doping, from fillings such as zinc,[14] copper[15] and cadmium halides[16] being demonstrated. Another hypothesized interaction that has received some experimental verification[17] is that electrostatic interactions between ionic fillings and electrons in the nanotube could alter the local electronic bandstructure of the tubes. There is a significant body of work on magnetic nanowires including Fe[18] and Co[19] and EuI_3.[20] Only limited research has been done on the applications of filled tubes, but this includes investigations into their applications as photothermal nanomaterials[21] and magnetic resonance imaging (MRI) contrast agents.[22] The large number of papers on the unfilled carbon nanotube composites and applications and the growing practicality of separation of nanotube types[23,24] strongly suggest that further applications will emerge as we better understand both the production and properties of the wide range of possible filled tubes.

A technique that has made a huge contribution to the study of SWCNTs is Raman scattering.[25] For filled SWCNTs this technique could potentially provide a rapid, nondestructive method of characterizing both type and quality of fillings as well as providing analytical information about the host tubes. In addition it would allow both phonon and optical transitions energies to be determined.[26] It can, when supported by theory, allow electron−phonon coupling to be quantified,[27] and time-resolved Raman can be used to probe phonon−phonon coupling.[28] Despite this, the application of Raman scattering to filled tubes has been relatively limited. The majority of work done so far has focused on the effect of filling on the Raman spectra of the host tubes.[29,30] An extensive search has led to only two papers in which some of the Raman features observed can be attributed to extended crystalline fillings (Te filling[31] and PbO filling[32]). In neither case was the resonance behavior of the filling features observed. This paper focuses on Raman spectroscopy of HgTe fillings within SWCNTs. We previously showed, using a combination of HRTEM and density functional theory (DFT), that a new low dimensional form of this material consisting of ∼1 nm tubular nanowires transforms from a semimetal (*i.e.*, bulk) to a semiconductor.[4] While there has been one previous report of Raman spectra from HgTe filled carbon nanotubes, in this case filled double walled tubes,[33] these results focused on the effects of filling on the temperature dependent frequency of the G and D band phonons of the host double walled tubes but did not present any features associated with the vibrations of the filling. We present here, for the first time Raman spectra from filled tube samples that present features clearly attributable to phonons of the HgTe filling and the dependence of these on the laser excitation energy and temperature.

RESULTS AND DISCUSSION

Filled tube samples were prepared by melt infiltration (see Supporting Information for synthetic details) using single walled tubes from two sources, arc-grown SWCNTs produced and purified by the protocols described by Krestinin *et al.*,[34] and NI96 "PureTubes" purified and supplied by NanoIntegris. The unfilled tubes were characterized using HRTEM which indicated that the vast majority of SWCNTs (>90%) in both samples had a median diameter in the range 1.2−1.6 nm, with the majority of the remainder deviating typically only by a maximum of 0.5 nm from this range. A few significantly larger diameter SWCNTs were observed in both samples with diameters up to ∼5 nm; however, these were rare and no reliable distribution of sizes could be determined.

After encapsulation and purification the filled tube samples were surveyed using HRTEM and their composition determined using energy dispersive X-ray (EDX) analysis (see Supporting Information for experimental details and EDX results). The EDX analysis gave a one to one ratio for the content of Hg to Te throughout all the samples. Our previous work found that the dominant form of HgTe filling found in filled tube samples was the low-dimensional tubular form of HgTe as depicted in Figure 1a.[4] For purposes of confirming the microstructure of the embedded HgTe nanocrystals, it is necessary to simulate the appearance of the tubular form of this material at different rotation angles and also at small tilt angles due to the low symmetry of the structure and also due to the sample sometimes being nonorthogonal with respect to the electron beam.[4] In Figure 1(b) (LH panel) we show a series of multislice image simulations performed for optimum defocus conditions for our instrument (*i.e.*, C_s = 0.001 mm, 80 kV accelerating voltage, defocus ∼7 nm) for a ∼3.1 nm long fragment of tubular HgTe as a function of axial rotation performed at 10° intervals up to a total rotation of 80° relative to an arbitrary starting orientation as defined by the structure model in Figure 1(a). The effect of tilting the sample is also simulated by applying a small 10° tilt as indicated in Figure 1(b), RH panel. Tilting the model in the opposite

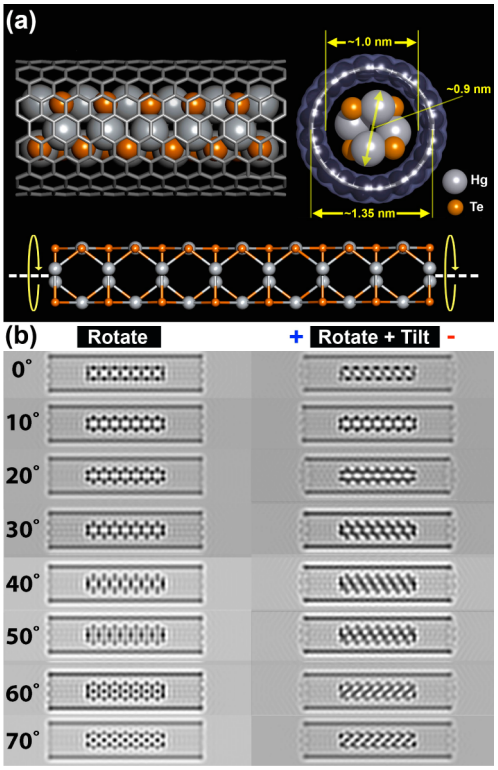

Figure 1. (a) (Top) Composite side- and end-on structure models of the semiconducting tubular form of HgTe encapsulated within a ~1.35 nm diameter (10,10) SWCNT. The end-on model on the right indicates the typical dimensions of a tubular HgTe nanowire. The diameter is constrained to ~1 nm in diameter by the van der Waals surface of the SWCNT (in blue).[1,4] (Bottom) Ball-and-stick representation of the tubular HgTe structure without the SWCNT in the starting orientation (*i.e.*, 0°) as employed in the HRTEM multislice simulations in (b). Arrows indicate the rotational sense employed in the simulations. (b) Two series of multislice simulations obtained using aberration parameters representative for the ARM200F HRTEM (*i.e.*, C_3 = 0.001 mm, accelerating voltage = 80 kV). The left-hand series shows the effect on the obtained image contrast of rotating the tubular crystal about its growth axis. The right-hand series is identical except that the crystal is tilted 10° as indicated by the ± signs.

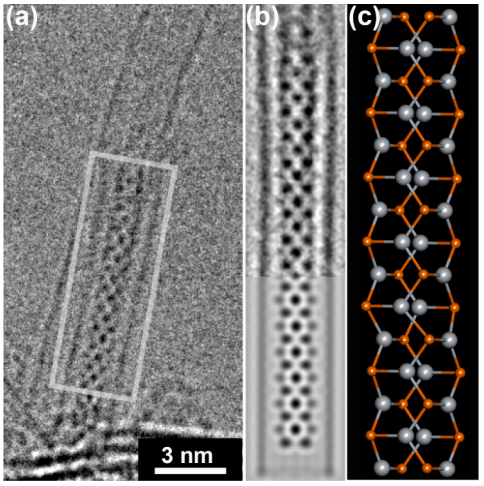

Figure 2. (a) HRTEM image of a discrete arc-grown SWCNT overlying a second empty SWCNT with an embedded HgTe tubular crystal fragment. (b) Enlarged Wien noise-filtered HRTEM image (top) obtained from the indicated region in (a) with a contiguous image simulation (bottom) obtained for a fragment with a 70° tilt as defined in (a) (left simulations). (c) Ball-and-stick representation of the HgTe microstructure corresponding to the images in (a) and (b). Note that the distinct black spots running along the center of the image and the simulations in (a) correspond to two slight staggered Hg atoms viewed in projection.

sense results in simulations with image contrast in a mirror image relationship to those reproduced in Figure 1(b).

The HRTEM survey showed a high fraction of the nanotubes were filled with HgTe nanocrystals whose predominant microstructure corresponds to the tubular form depicted in Figure 1(a). In Figure 2(a) we see a fragment of tubular HgTe imaged in a discrete SWCNT overlying a second unfilled SWCNT. The obtained microstructure (enlarged in Figure 2(b)) provides an excellent match with an image simulation (bottom, Figure 2(b)) that conforms to a 70° orientation of the tubular form as defined in Figure 1(a). A ball-and-stick model corresponding to this orientation (HgTe fragment only) is reproduced in Figure 2(c). In Figure 3(a–d) we give several further examples of HgTe filling microstructures observed in the sample. Often, in the case of high filling fraction SWCNTs (*e.g.*, Figure 3(a)), the microstructure of the filling is obscured by other embedded crystals above or below the imaged crystal. Some bundles were observed with only partial filling in which case structural identification was more straightforward. In Figure 3(b), we see a large bundle of SWCNTs with three regions with identifiable microstructure (*i.e.*, **I**, **II** and **III**). Details extracted from these fragments can all be correlated with microstructures reproduced in Figure 1(b). Fragments **I′** and **III′** can both be correlated with the 10° rotation depicted in Figure 1(b). Fragment **II′** is similar but is possibly slightly tilted within the bundle. A further example is given in Figure 3(c) of a discrete SWCNT containing a tubular HgTe fragment but which has a significant tilt (*ca.* 10°) with respect to the electron beam as can be seen from the corresponding detail and matching simulation (Figure 3(a) bottom, *cf.* 40° rotation, 10° tilt simulation RH panel, Figure 1(a)). In those rare instances when we observed wider filled SWCNTs, microstructures corresponding to bulk-like HgTe phases were observed. In Figure 3(d) we see that a fragment of rocksalt-like HgTe can be observed. This microstructure was identified from the corresponding FFT (inset) with (020) and (200) lattice spacing corresponding to the low temperature modification of this phase.[26]

Raman spectroscopy was performed with laser energies in two ranges, a blue range 2.61–3.31 eV and a red/IR range 1.26–1.82 eV, with spectral resolution of 1 cm^{-1} in the blue range and 0.5 cm^{-1} in the red range. The spectra presented in this paper were measured with the sample in a coldfinger in a vacuum (~10^{-6} mbar) at 4 K. The 4 K spectra are presented as these have the

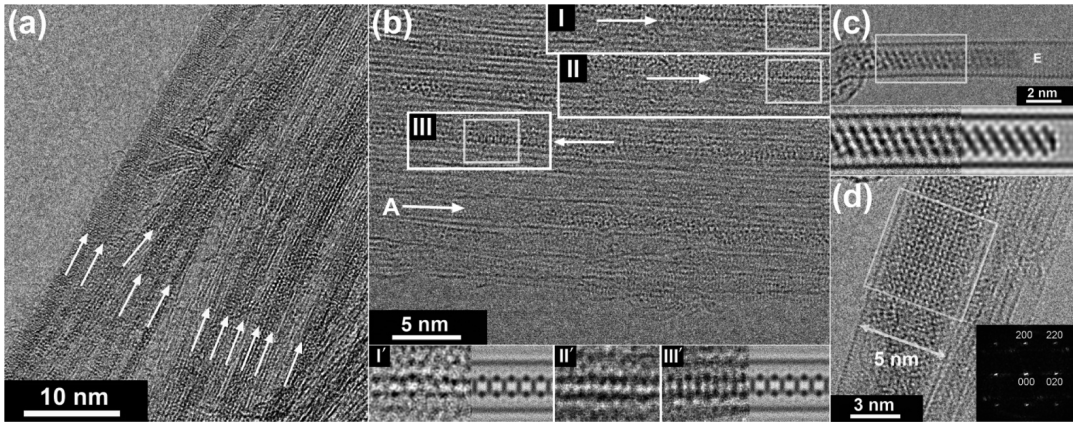

Figure 3. (a) Plan view image of a representative bundle of arc-grown SWCNTs filled in high yield (white arrows indicate filled SWCNTs) with HgTe. (b) Second plan-view image showing a SWCNT bundle with lower filling fraction than (a) but in which microstructures of the obtained filling are more clearly visible (*i.e.*, I, II and III). Apart from a small amorphous region (A) most of the observable crystals in this sample have tubular microstructures similar to Figures 1 and 2. Three details from the main image are presented at the bottom of (b), *i.e.*, I′, II′ and III′. Fragments I′ and III′ can be correlated with the 10° rotation simulation in Figure 1(b). Fragment II′ is similar but is possibly slightly tilted within the bundle (*cf.* tilted SWCNT "T" in (a)). (c) Tilted HgTe fragment in a partially filled SWCNT (empty region indicated by E). The observed filling microstructure corresponds to a 10° tilted fragment rotated by 40° (*cf.* RH Panel, Figure 2(b)). (d) Rare (<2%) 5 nm wide SWCNT containing a fragment of rocksalt-like HgTe (as indicated by the inset FFT).

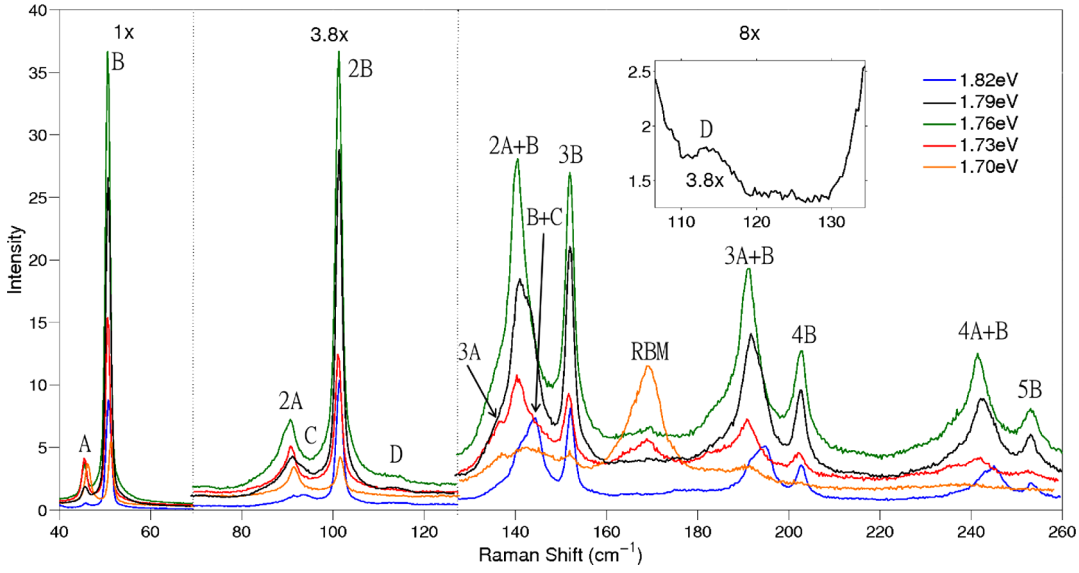

Figure 4. Representative Raman spectra of a HgTe@SWCNT sample for various laser excitation energies. The spectra have been split into three Raman shift ranges and their magnitude scaled by 1, 3.8, and 8 times as indicate on the figure. The inset shows a zoomed in section of the spectra in the range 105−136 cm^{-1} with magnitude scaled by 3.8. The labels for the Raman features are discussed in the main text.

clearest features; however, spectra measured over the range 4−300 K show no new features and no sudden or unusual changes in central frequency or width of the features and no significant change in the laser energy dependence of the spectra. A full analysis of the temperature dependence will be presented in a future publication. No sample degradation was observed during the experiments (see Supporting Information for further experimental details). The Raman spectra acquired on the two HgTe@SWCNT samples were remarkably similar, and all of the data support the conclusions of this paper, and therefore for simplicity we will present data from the sample prepared using tubes produced and purified by the method set out in Krestinin *et al.*[34] For excitation laser energies in the high (blue) energy range and for laser energies lower than 1.64 eV in the low (red/IR) range the only Raman features observed were all present in spectra from the parent unfilled tubes. However, in the excitation energy range 1.64−1.84 eV a number of additional Raman features were observed with Raman shifts in the 40−300 cm^{-1} range, which are presented in Figure 4. The only feature present in these spectra that is also present in the parent unfilled tube spectra is at 170 cm^{-1}. This mode has a Stokes resonance (Figure 5) at 1.676 eV and we attribute it as a radial breathing mode (RBM) of a 1.43 ± 0.03 nm

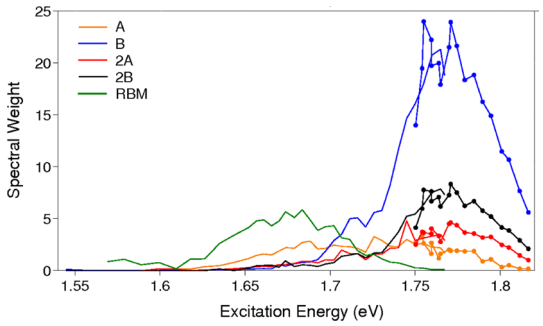

Figure 5. Excitation energy dependence of the spectral weight of various Raman features. The spectral weight was determined by fitting Lorentzian line shapes to the Raman features and determining the integrated intensity associated with each feature.

diameter metallic nanotube.[35] The other Raman features were observed in all of the filled tube samples. These features are very similar to the multiphonon spectra often seen with inorganic semiconductors such as HgTe[36] and ZnO,[37] which have been shown to be enhanced in nanowire structures.[38] In particular the two lowest energy peaks, at 47 cm^{-1} (peak A) and 51 cm^{-1} (peak B), are associated with two higher energy peaks at precisely twice the energy to within experimental error (labeled 2A and 2B on Figure 4). The next group of Raman features, in the range 130−160 cm^{-1}, has clear peaks at energies 3B and 2A+B. In addition there is a feature seen in the 1.703 eV excited spectra which is at an energy of 3A. However, in the higher excitation energy spectra it is very clear that there is an additional peak at 144.5 cm^{-1} that cannot be a combination of the A and B modes. Careful consideration of the second band of Raman features shows that there is a third peak close to the 2A feature which dominates over the 2A peak at higher excitation energies. This peak is at 94 cm^{-1} and is labeled C and the combination of this mode with a single B mode can explain the peak at 144.5 cm^{-1}. There are least two more higher frequency bands of Raman features in which all the major features can be explained as combinations of the excitations responsible for the A, B and C Raman features. The only non-RBM mode that cannot easily be explained using these three excitations is a very small feature centered at 115 cm^{-1} labeled D. It is not possible to observe any features that are a harmonic of the excitation responsible for this mode or a combination of this excitation with any of the other excitations; however, this may be due to it not being strongly Raman active.

We investigated the polarization dependence of the Raman scattering and how this depended on the polarization of the incoming light. We found that all of the Raman features had the same polarization dependence, with Raman scattering occurring preferentially in the direction of the incoming polarization with a contrast ratio of between 2:1 and 4:1 in the manner expected for nanowire like objects (see Supporting Information).

In order to understand the Raman spectra better the excitation energy dependence of the Raman spectra were measured with ∼5 meV resolution over the range 1.64−1.818 eV. The spectra obtained were fitted using Lorentzian lineshapes for each of the modes already discussed. The central frequency or line width have no significant variation with excitation energy. The excitation energy dependences of the spectral weight (area of peak) of various significant peaks are presented in Figure 5. The resonance profiles shown on Figure 5 can be separated into 4 main groups. The RBM mode has a relatively symmetric resonance centered at 1.676 eV with width (fwhm) 70 meV. The A mode resonance is also relatively symmetric, is centered at 1.722 eV with a width (fwhm) of 120 meV. The B, 2A, 2B modes have resonances that consist of a main peak centered at 1.759 eV with a width (fwhm) of 80 meV plus a low energy tail that extends to ∼1.664 eV. As the C mode feature is very close to the 2A feature it is difficult to separate its resonance profile, and the fitting was not stable. However, this Raman feature is clearly resonant in the same basic energy range as the A and B features. It is also clear that the C mode resonance is shifted to slightly higher energy than the 2A resonance by consideration of the relative strength of the 2A and C modes in the spectra presented in Figure 4. The D mode is only clearly observable in the energy range 1.82 to 1.766 eV; however, it was too weak to extract a clear resonance profile.

The most important question to be considered concerning the data is what component of the samples is responsible for the Raman features observed. The non-RBM features are only seen in HgTe@SWCNT samples. As these modes are only seen in HgTe filled tube samples it is likely that they are associated with HgTe filling or any extraneous HgTe material. We have observed no elemental Hg or Te bulk or nanostructures in the material by TEM. The Raman spectrum of bulk zinc blende HgTe[39] consists of three basic peaks, two at 117 and 137 cm^{-1}, which are attributed[40] to the zone center TO and LO phonon modes respectively, and a third mode that has a strongly temperature dependent magnitude and energy (110 cm^{-1} at 293 and 97 cm^{-1} at 4 K) which is attributed to a combination mode. Therefore, we can be confident that the HgTe@SWCNT Raman spectra are not due to bulk-like HgTe residue in the sample. Thus, we can conclude that the Raman features are due to HgTe nanostructures and in particular nanowires or quantum dots. There have been a number of studies of the Raman spectra of HgTe quantum dots[2] and related colloidal semiconductor particles.[1] These studies have found that for nanoparticles with diameters less than ≈6 nm new Raman modes attributed to confined acoustic modes, zone edge phonons and surface optical phonons do occur. However, even for the smallest nanoparticles studied, 2 nm diameter, the Raman spectra are dominated by

TABLE 1. DFT-Predicted Γ Point Phonon Mode Energies and Symmetry

E (cm^{-1})	sym	E (cm^{-1})	sym
5.1	A_g	107.2	E_u
15	B_g	110.4	A_u
21.2	E_g	112.7	B_g
27.5	B_u	121.3	E_g
36.7	B_g	130.5	B_u
53.68	A_g	132.7	A_g
53.74	E_u	148.4	B_g
106.5	A_g	149.1	E_u

the LO phonon whose frequency is slightly shifted from the bulk. Thus, we can conclude that the modes observed in the filled tube samples are due to nanostructures with at least one dimension smaller than 2 nm. The TEM investigations of the samples clearly demonstrate that the most likely candidate are the in-tube nanowires. This hypothesis is further supported by the polarization dependence of the Raman features. In particular it is possible to show that for a sample of randomly oriented, straight, noninteracting nanowires which, as expected due to depolaristion effects, interact with and emit light only parallel to the nanowires one that the Raman scattered light should be preferentially polarized parallel to the excitation light with a contrast ratio of 3:1. While the observed contrast ratios are not precisely 3:1 this can easily be understood by bundling, leading to nonrandom orientation and interaction of the local fields of nanowires or bundles in close proximity.

In order to investigate if the Raman results were consistent with the observed HgTe nanowire structure we undertook *ab initio* calculations of the vibrational modes and optical absorption spectrum expected for this structure (see Methods[41−43]). On the basis of the HRTEM observations, DFT calculations were performed by taking a Hg_4Te_4 unit cell belonging to the rod group #29, $p4_2/m$, with point group symmetry C_{4h} and a translation vector length along the chain axis of 0.446 nm (see Supporting Information for further details). The bond lengths and bond angles calculated are in good agreement with the structure experimentally found by HRTEM (see Supporting Information).

The predicted Γ phonon mode energies are given in Table 1 along with their symmetries. Representations of the atomic motions for each of the predicted modes along with predicted dispersion relations are given in the Supporting Information. As expected by symmetry there are 15 vibrational modes including 2 doubly degenerate E_g and 3 doubly degenerate E_u symmetry modes. The first Raman allowed mode of A_g symmetry should have zero frequency for a free-standing rod as it represents rotation about the rod axis. However, the calculation is performed for a 3-D supercell giving a weak frequency for this mode. The nonresonant Raman selection rules predict that all but the E_u and

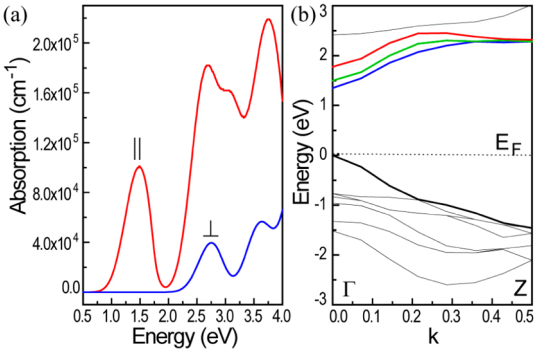

Figure 6. DFT predictions of the (a) optical absorbance spectra for light parallel and perpendicular to the filled tube and (b) electronic dispersion relations for the single electron bands nearest the Fermi energy.

B_u modes should be Raman active; however, as the spectra are taken under strongly resonant conditions these rules probably do not apply. Currently prediction of resonant Raman spectra for nonmolecular systems is not feasible using standard computing resources. The three lowest frequency predicted modes could not be observed in our experiments as they are too close to the laser line. The modes with energies greater than ∼130 cm^{-1} could be present but covered by the third order harmonic and combinations peaks. This leaves eight DFT predicted phonons which may be responsible for the four observed Raman peaks. It is quite likely that only some of the predicted modes are strongly resonantly enhanced. Most of the observed Raman peaks can be attributed to separate predicted modes with errors of less than 10%. More concretely, the calculated modes at ∼37 cm^{-1} (B_g) and ∼54 cm^{-1} (A_g), comprising of Hg atomic motion against each other in the *xy*-plane and the low frequency modes which lead to the largest changes in interatomic spacing, are plausible candidates for the generic A and B features in the resonant Raman spectra. The more significant wavenumber difference between the lower frequency mode and the A peak could be ascribed to the interaction between the HgTe nanorod and the surrounding nanotube, which is not accounted for in our calculations. The calculated B_g mode at ∼113 cm^{-1} fits precisely the weak D feature, which cannot otherwise be explained as a combination or overtone. However, as with the A and B modes, this assignment is not unambiguous.

On Figure 6 we present our predictions of the electron band dispersion and the optical absorption constant associated with the predicted bands. It should be noted that the prediction is based on the Kohn−Sham orbitals and do not include electron−hole correlation effects, *i.e.*, excitonic binding energies. These results indicate that there are three conduction bands, which are close in energy, into which electrons can be excited from the valence band by dipole allowed transitions. Because of computational constraints the calculation cannot reproduce the singularities that

should be associated with these transitions; however, from the band dispersions we can predict that there are three possible Raman resonances at 1.35, 1.5, and 1.75 eV and others at energies in excess of 2.5 eV. The calculations predict that the three lower energy transitions are strongly polarized, parallel to the filled tube.

Experimentally all of the filling Raman features show strong resonances and cannot be detected apart from with excitation laser energies within a relatively narrow band around 1.76 eV. It is presumably for this reason that the other Raman studies on HgTe filled tubes have not observed Raman scattering from the HgTe filling.[33] Clearly the DFT calculations provide a number of candidates for what the resonant transitions is. It is possible, within the accuracy of the calculations, that we are resonant with the fundamental bandgap in the filling, which would explain why we only observe a single resonance in the red range; however, we cannot be sure of this. It should be noted that the DFT predictions suggest there should be a resonance in the blue laser energy range which we do not observe.

In principle the width and shape of the resonances contains additional important information. In the case of bulk inorganic semiconductors resonance profiles of one phonon Raman peaks have been used to determine the importance and strength of different electron–phonon coupling mechanisms and how these vary between different high symmetry points in the bandstructure.[44] Two phonon resonance profiles give additional information about the interference of scattering pathways involving different electronic states,[45] *e.g.*, free carrier and excitonic. When considering the resonance behavior reported here it is important to keep in mind that the width of the resonance is much greater than the energies of the fundamental Raman features, *i.e.*, A, B, C and D, and even broader than the Raman shifts of the combination peaks. Thus, the resonance observed is an overlap of incoming, outgoing and intermediate state resonances. As already described the resonance profiles of the A and B modes are not the same shape. This may be attributable to substructure within the electronic states responsible for the resonance. It might be tempting to suggest that the low energy tail of the B mode resonance and the A mode resonance are both related to electronic states which generate a broader resonance at 1.71 ± 0.03 eV and that the excitation responsible for the B feature is also able to couple to another electronic state, which generates a narrower, slightly higher energy resonance at 1.76 ± 0.01 eV. However, we cannot be sure of this interpretation without further theoretical work.

CONCLUSION

In conclusion, in this paper we present a resonance Raman study of single walled carbon nanotubes filled with HgTe. The measured Raman spectra contain a large number of features which are not observed in spectra of unfilled carbon nanotubes. These can be separated into four fundamental modes at 47, 51, 94, and 115 cm^{-1} plus the overtones and combinations of the first three fundamental modes. These features are not consistent with the Raman spectra of bulk HgTe or HgTe nanoparticles with diameters greater than 2 nm. The polarization dependencies of the 47 and 51 cm^{-1} Raman features are consistent with these modes being due to nanowires; the other two fundamental modes polarization dependencies are not measurable. All of the modes exhibit photon energy resonances at around 1.76 eV. For the stronger, lowest frequency two modes and their second harmonics we have measured clear resonance profiles. Future theoretical interpretation of these resonances may allow us to better understand the electronic states involved in the resonances and/or further details of the electron–phonon interaction. We have performed DFT calculations, which do not include excitonic effects, based upon the structure of the HgTe nanowires observed by TEM. These are consistent with both the measured shifts of the Raman features and the Resonance energy to within reasonable errors. These calculations predict a bandgap for the HgTe wires of 1.35 eV; however, they also predict other optical transitions at energies of 1.5 and 1.75 eV that are candidates for the resonant optical transition. We believe these measurements are the first time anyone has published the Raman spectra of HgTe nanowires formed inside carbon nanotubes. We believe these results demonstrate clearly the need for the initial Raman studies on filled tubes to be performed using a tunable laser based Resonance Raman system. For preference this should be based upon a triple grating spectrometer to allow the detection of low frequency Raman peaks which are more common in filled tubes due to their reduced coordination and the reduction of translational symmetry in 1D systems leading to more Raman accessible vibrational modes. Now that we have determined the resonance energy for HgTe fillings it would be possible to setup a cheaper, higher throughput Raman system to enable routine characterization of filled HgTe tubes, which will make exploiting them in applications such as photovoltaics and saturable absorbers for ultrafast lasers easier.

METHODS

Synthesis of HgTe Filled SWNTs. The filling protocol involved mixing 20 mg of dry SWNTs (*i.e.*, either supplied SWNTs from Krestinin *et al.*[34] or Nanointegris NI96 SWNTs) together with half of the same volume of HgTe (VMR 99.999%, metals basis) in a pestle and mortar under an argon atmosphere in a glovebox

with grinding for *ca.* 20 min. The mix of guest material and SWNT was then inserted into a silica quartz ampules that were sealed under a vacuum and then heated in a Carbolite muffle furnace to *ca.* 770 °C with thermal cycling ±100 °C (12 h intervals) relative to the melting temperature of HgTe (*i.e.*, 670 °C) for a total heating time of 48 h. The as-prepared composites were dispersed ultrasonically in ethanol for HRTEM imaging and Raman investigations.

HRTEM Investigations and Simulations. A JEM-ARM 200F microscope operating at 80 kV equipped with a CEOS aberration corrector and a Gatan SC1000 ORIUS camera with a 4008 × 2672 pixel charge-coupled device (CCD) was used for TEM investigations. Dispersions of HgTe/SWNT nanocomposites were drop cast onto 3.05 mm Cu specimen support grids (Agar Scientific) prior to HRTEM investigations. Energy dispersive X-ray studies were performed in the ARM 200F HRTEM using a ~1 nm diameter probe focused onto filled bundles of SWNTs. Spectra were recorded using an Oxford Instruments SDD X-ray microanalysis detector. Structure models were assembled using CrystalMaker (Version 8) software and standard Shannon anion and cation radii. Nanotube models for the composite models and HRTEM simulations were produced using Nanotube Modeler from JCrystalSoft (2005–2013). Image simulations were performed from density functional theory (DFT) refined structural data for the HgTe nanocrystal[4] using the multislice package SimulaTEM.

Density Functional Theory Calculations. The calculations were performed with the CASTEP[41] code, using density functional perturbation theory (DFPT)[42] within the generalized gradient approximation scheme (GGA) with the Perdew–Burke–Ernzerhof (PBE) exchange-correlation functional.[43] On the basis of the HRTEM observations, DFT calculations were performed by taking a Hg_4Te_4 unit cell belonging to the rod group #29, $p4_2/m$, with point group symmetry C_{4h} and a translation vector length along the chain axis of 0.446 nm (see Supporting Information for further details).

Raman Spectroscopy. The Raman experiments were performed using a Coherent MIRA Ti:sapphire laser operated in continuous wave mode in the spectral range 680–980 nm and using frequency doubles 2–3 ps pulses in the range 375–475 nm. In the long wavelength region the laser light was filtered by either a Photonetc TLS 850 filter (between 700 and 980 nm) or an Opti-Grate volume Bragg grating (680–710 nm). Samples were drop cast onto 200 nm thick oxide coated silicon chips and held in an Oxford Instruments microstat He flow cryostat at a vacuum of 6×10^{-6} mbar. Raman spectra were taken using a back scattering setup through an Olympus LMPan IR 50× microscope objective. The backscattered light was coupled into a Princeton Instruments TriVista triple 600 nm spectrometer equipped with a Princeton Instruments deep depleted, UV enhanced, liquid N_2 cooled silicon CCD. Please see Supporting Information for further details.

Conflict of Interest: The authors declare no competing financial interest.

Acknowledgment. J.S. and R.J.K. are indebted to the Warwick Centre for Analytical Science (EPSRC funded Grant EP/F034210/1). Additionally, we are indebted to Drs. Zheng Liu and Kazu Suenaga who provided panel (a) of Figure 2, which originally appeared in *Microsc. Semicond. Mater.* **2008**, *120*, 213–216 (used with permission). Calculations were performed at Centre de Calcul Intensif des Pays de la Loire (CCIPL), University of Nantes. V.G.I. thanks the University of Nantes for a short-term position as invited professor. This research was partly funded by EPSRC, UK *via* grants EP/C006763/1 and EP/I033394/1.

Supporting Information Available: Details of the HRTEM and Raman experimental systems and methods; details of the DFT calculation methods; complete set of resonance Raman spectra at 4 K; representative Raman spectra obtained on all two samples; optimized bond lengths and angles, phonon atomic displacements, nonresonant Raman spectra and phonon dispersion and density of states predicted by DFT. This material is available free of charge *via* the Internet at http://pubs.acs.org.

REFERENCES AND NOTES

1. Sloan, J.; Hammer, J.; Zwiefka-Sibley, M.; Green, M. L. H. The Opening and Filling of Single Walled Carbon Nanotubes (SWTs). *Chem. Commun.* **1998**, 347–348.
2. Sloan, J.; Kirkland, A. I.; Hutchison, J. L.; Green, M. L. H. Integral Atomic Layer Architectures of 1D Crystals Inserted into Single Walled Carbon Nanotubes. *Chem. Commun.* **2002**, 1319–1332.
3. Sloan, J.; Grosvenor, S. J.; Friedrichs, S.; Kirkland, A. I.; Hutchison, J. L.; Green, M. L. H. A One-Dimensional BaI2 Chain with Five- and Six-Coordination, Formed within a Single-Walled Carbon Nanotube. *Angew. Chem., Int. Ed.* **2002**, *41*, 1156–1159.
4. Carter, R.; Sloan, J.; Kirkland, A. I.; Meyer, R. R.; Lindan, P. J. D.; Lin, G.; Green, M. L. H.; Vlandas, A.; Hutchison, J. L.; Harding, J. Correlation of Structural and Electronic Properties in a New Low-Dimensional form of Mercury Telluride. *Phys. Rev. Lett.* **2006**, 96.
5. Derouane, E. G. Zeolites as Solid Solvents. *J. Mol. Catal. A: Chem.* **1998**, *134*, 29–45.
6. Alba-Simionesco, C.; Coasne, B.; Dosseh, G.; Dudziak, G.; Gubbins, K. E.; Radhakrishnan, R.; Sliwinska-Bartkowiak, M. Effects of Confinement on Freezing and Melting. *J. Phys.: Condens. Matter* **2006**, *18*, R15–R68.
7. Ke, J.; Su, W.; Howdle, S. M.; George, M. W.; Cook, D.; Perdjon-Abel, M.; Bartlett, P. N.; Zhang, W.; Cheng, F.; Levason, W.; Reid, G.; Hyde, J.; Wilson, J.; Smith, D. C.; Mallik, K.; Sazio, P. Electrodeposition of Metals from Supercritical Fluids. *Proc. Natl. Acad. Sci. U. S. A.* **2009**, *106*, 14768–14772.
8. Lu, G.; Li, S.; Guo, Z.; Farha, O. K.; Hauser, B. G.; Qi, X.; Wang, Y.; Wang, X.; Han, S.; Liu, X.; DuChene, J. S.; Zhang, H.; Zhang, Q.; Chen, X.; Ma, J.; Loo, S. C. J.; Wei, W. D.; Yang, Y.; Hupp, J. T.; Huo, F. Imparting Functionality to a Metal-Organic Framework Material by Controlled Nanoparticle Encapsulation. *Nat. Chem.* **2012**, *4*, 310–316.
9. Alvarez, L.; Bantignies, J. L.; Le Parc, R.; Aznar, R.; Sauvajol, J. L.; Merlen, A.; Machon, D.; San Miguel, A. High-Pressure Behavior of Polyiodides Confined into Single-Walled Carbon Nanotubes: A Raman Study. *Phys. Rev. B: Condens. Matter Mater. Phys.* **2010**, 82.
10. Giusca, C. E.; Stolojan, V.; Sloan, J.; Börrnert, F.; Shiozawa, H.; Sader, K.; Rümmeli, M. H.; Büchner, B.; Silva, S. R. P. Confined Crystals of the Smallest Phase-Change Material. *Nano Lett.* **2013**, *13*, 4020–4027.
11. Fan, X.; Dickey, E. C.; Eklund, P. C.; Williams, K. A.; Grigorian, L.; Buczko, R.; Pantelides, S. T.; Pennycook, S. J. Atomic Arrangement of Iodine Atoms Inside Single-Walled Carbon Nanotubes. *Phys. Rev. Lett.* **2000**, *84*, 4621–4624.
12. Park, T.; Sim, K.; Lee, J.; Yi, W. Electron Transfer Properties of Iodine-Doped Single-Walled Carbon Nanotubes Using Field Effect Transistor. *J. Nanosci. Nanotechnol.* **2012**, *12*, 5812–5815.
13. Chamberlain, T. W.; Biskupek, J.; Rance, G. A.; Chuvilin, A.; Alexander, T. J.; Bichoutskaia, E.; Kaiser, U.; Khlobystov, A. N. Size, Structure, and Helical Twist of Graphene Nanoribbons Controlled by Confinement in Carbon Nanotubes. *ACS Nano* **2012**, *6*, 3943–3953.
14. Kharlamova, M. V.; Yashina, L. V.; Volykhov, A. A.; Niu, J. J.; Neudachina, V. S.; Brzhezinskaya, M. M.; Zyubina, T. S.; Belogorokhov, A. I.; Eliseev, A. A. Acceptor Doping of Single-Walled Carbon Nanotubes by Encapsulation of Zinc Halogenides. *Eur. Phys. J. B* **2012**, 85.
15. Kumskov, A. S.; Zhigalina, V. G.; Chuvilin, A. L.; Verbitskiy, N. I.; Ryabenko, A. G.; Zaytsev, D. D.; Eliseev, A. A.; Kiselev, N. A. The Structure of 1D and 3D CuI Nanocrystals Grown Within 1.5–2.5 nm Single Wall Carbon Nanotubes Obtained by Catalyzed Chemical Vapor Deposition. *Carbon* **2012**, *50*, 4696–4704.
16. Kharlamova, M. V.; Yashina, L. V.; Lukashin, A. V. Charge Transfer in Single-Walled Carbon Nanotubes Filled with Cadmium Halogenides. *J. Mater. Sci.* **2013**, *48*, 8412–8419.
17. Ilie, A.; Bendall, J. S.; Nagaoka, K.; Egger, S.; Nakayama, T.; Crampin, S. Encapsulated Inorganic Nanostructures: A Route to Sizable Modulated, Noncovalent, On-Tube

Potentials in Carbon Nanotubes. *ACS Nano* **2011**, *5*, 2559–2569.
18. Grobert, N.; Hsu, W. K.; Zhu, Y. Q.; Hare, J. P.; Kroto, H. W.; Walton, D. R. M.; Terrones, M.; Terrones, H.; Redlich, P.; Ruhle, M.; Escudero, R.; Morales, F. Enhanced Magnetic Coercivities in Fe Nanowires. *Appl. Phys. Lett.* **1999**, *75*, 3363–3365.
19. Yang, C. K.; Zhao, J.; Lu, J. P. Magnetism of Transition-Metal/Carbon-Nanotube Hybrid Structures. *Phys. Rev. Lett.* **2003**, 90.
20. Fidiani, E.; Costa, P.; Wolter, A. U. B.; Maier, D.; Buechner, B.; Hampel, S. Magnetically Active and Coated Gadolinium-Filled Carbon Nanotubes. *J. Phys. Chem. C* **2013**, *117*, 16725–16733.
21. Rossella, F.; Soldano, C.; Bellani, V.; Tommasini, M. Metal-Filled Carbon Nanotubes as a Novel Class of Photothermal Nanomaterials. *Adv. Mater.* **2012**, *24*, 2453–2458.
22. Zhang, Z. D. Magnetic Nanocapsules. *J. Mater. Sci. Technol.* **2007**, *23*, 1–14.
23. Li, X.; Tu, X.; Zaric, S.; Welsher, K.; Seo, W. S.; Zhao, W.; Dai, H. Selective Synthesis Combined with Chemical Separation of Single-Walled Carbon Nanotubes for Chirality Selection. *J. Am. Chem. Soc.* **2007**, *129*, 15770–15771.
24. Krupke, R.; Hennrich, F.; von Lohneysen, H.; Kappes, M. M. Separation of Metallic from Semiconducting Single-Walled Carbon Nanotubes. *Science* **2003**, *301*, 344–347.
25. Dresselhaus, M. S.; Dresselhaus, G.; Saito, R.; Jorio, A. Raman Spectroscopy of Carbon Nanotubes. *Phys. Rep.* **2005**, *409*, 47–99.
26. Araujo, P. T.; Pesce, P. B. C.; Dresselhaus, M. S.; Sato, K.; Saito, R.; Jorio, A. Resonance Raman Spectroscopy of the Radial Breathing Modes in Carbon Nanotubes. *Phys. E* **2010**, *42*, 1251–1261.
27. Calleja, J. M.; Cardona, M. Resonant Raman-Scattering in ZnO. *Phys. Rev. B: Solid State* **1977**, *16*, 3753–3761.
28. Nesbitt, J. M.; Smith, D. C. Measurements of the Population Lifetime of D Band and G′ Band Phonons in Single-Walled Carbon Nanotubes. *Nano Lett.* **2013**, *13*, 416–422.
29. Eliseev, A. A.; Yashina, L. V.; Verbitskiy, N. I.; Brzhezinskaya, M. M.; Kharlamova, M. V.; Chernysheva, M. V.; Lukashin, A. V.; Kiselev, N. A.; Kumskov, A. S.; Freitag, B.; Generalov, A. V.; Vinogradov, A. S.; Zubavichus, Y. V.; Kleimenov, E.; Nachtegaal, M. Interaction Between Single Walled Carbon Nanotube and 1D Crystal in CuX@SWCNT (X = Cl, Br, I) Nanostructures. *Carbon* **2012**, *50*, 4021–4039.
30. Liu, S. W.; Zhu, J. J.; Mastai, Y.; Felner, I.; Gedanken, A. Preparation and Characteristics of Carbon Nanotubes Filled with Cobalt. *Chem. Mater.* **2000**, *12*, 2205–2211.
31. Belandria, E.; Millot, M.; Broto, J.-M.; Flahaut, E.; Rodriguez, F.; Valiente, R.; Gonzalez, J. Pressure Dependence of Raman Modes in Double Wall Carbon Nanotubes Filled with 1D Tellurium. *Carbon* **2010**, *48*, 2566–2572.
32. Hulman, M.; Kuzmany, H.; Costa, P.; Friedrichs, S.; Green, M. L. H. Light-Induced Instability of PbO-Filled Single-Wall Carbon Nanotubes. *Appl. Phys. Lett.* **2004**, *85*, 2068–2070.
33. Sendova, M.; Flahaut, E.; Hartsfield, T. Temperature Dependence of Raman Scattering in Filled Double-Walled Carbon Nanotubes. *J. Appl. Phys.* **2010**, 108.
34. Krestinin, A. V.; Kiselev, N. A.; Raevskii, A. V.; Ryabenko, A. G.; Zakharov, D. N.; Zvereva, G. I. Perspective of Single-Wall Carbon Nanotube Production in the Arc-Discharge. *Eurasian Chem.-Technol. J.* **2005**, *5*, 7–18.
35. Cheng, Q.; Debnath, S.; Gregan, E.; Byrne, H. J. Vibrational Mode Assignments for Bundled Single-Wall Carbon Nanotubes using Raman Spectroscopy at Different Excitation Energies. *Appl. Phys. A: Mater. Sci. Process.* **2011**, *102*, 309–317.
36. Rosch, M.; Atzmuller, R.; Schaack, G.; Becker, C. R. Resonant Raman-Scattering in a Zero-Gap Semiconductor-Interference Effects and Deformation Potentials at the E(1) and E(1)+Delta(1) Gaps of HgTe. *Phys. Rev. B: Condens. Matter Mater. Phys.* **1994**, *49*, 13460–13474.
37. Huso, J.; Morrison, J. L.; Mitchell, J.; Casey, E.; Hoeck, H.; Walker, C.; Bergman, L.; Oo, W. M. H.; McCluskey, M. D. Optical Transitions and Multiphonon Raman Scattering of Cu Doped ZnO and MgZnO Ceramics. *Appl. Phys. Lett.* **2009**, 94.
38. Brewster, M.; Schimek, O.; Reich, S.; Gradecak, S. Exciton-Phonon Coupling in Individual GaAs Nanowires Studied using Resonant Raman Spectroscopy. *Phys. Rev. B: Condens. Matter Mater. Phys.* **2009**, 80.
39. Ingale, A.; Bansal, M. L.; Roy, A. P. Resonance Raman-Scattering in HgTe -To- Phonon and Forbidden-LO-Phonon Cross-Section Near the E1 Gap. *Phys. Rev. B: Condens. Matter Mater. Phys.* **1989**, *40*, 12353–12358.
40. Bansal, M. L.; Ingale, A.; Roy, A. P. Anomalous Mode in the Raman and IR-Spectra of Mercury Telluride. *Phys. Rev. B: Condens. Matter Mater. Phys.* **1991**, *43*, 7020–7026.
41. Clark, S. J.; Segall, M. D.; Pickard, C. J.; Hasnip, P. J.; Probert, M. J.; Refson, K.; Payne, M. C. First Principles Methods Using CASTEP. *Z. Kristallogr.* **2005**, *220*, 567–570.
42. Refson, K.; Tulip, P. R.; Clark, S. J. Variational Density-Functional Perturbation Theory for Dielectrics and Lattice Dynamics. *Phys. Rev. B: Condens. Matter Mater. Phys.* **2006**, 73.
43. Perdew, J. P.; Burke, K.; Ernzerhof, M. Generalized Gradient Approximation Made Simple. *Phys. Rev. Lett.* **1996**, *77*, 3865–3868.
44. Kauschke, W.; Cardona, M. Resonant Raman-Scattering and Interference Effects of LO Phonons at the E0+Delta-0 Gap of InP. *Phys. Rev. B: Condens. Matter Mater. Phys.* **1986**, *33*, 5473–5481.
45. Garciacristobal, A.; Cantarero, A.; Tralleroginer, C.; Cardona, M. Excitonic Model for 2nd-Order Resonant Raman-Scattering. *Phys. Rev. B: Condens. Matter Mater. Phys.* **1994**, *49*, 13430–13445.